

Performance Analysis of Varying Central Shaft Diameters on Cross-flow Hydrokinetic Turbines

University of Washington

Mechanical Engineering Department

Senior Capstone Design Project

Winter 2019

Advisors:

Brian Polagye

Rob Cavagnaro

Students:

Aidan Hunt

Cassie Riel

Christopher Campbell

Cody Hotchkiss

Zack Tully

Table of Contents

Motivation	3
Method	3
Equipment	3
Experimental Design	5
Reynolds Number Dependence	6
Experimental Procedure	7
Data Analysis	7
Results	8
Test Equipment Performance	8
Performance vs Shaft Blockage Ratio	9
Reynolds Dependence	12
Phase Average Performance	13
Performance Variations with Blade Count	15
Discussion	16
Sources of Error/Uncertainty	16
Environmental Impact	17
Societal Impact	18
Economic Analysis	18
Risk and Liability	19
Ethics	19
Conclusion	19
References	20
Appendix A: Design	22
Concept Generation	22
Materials Selection	23
Design Calculations	23
PVC beam bending	23
Rubber compression	27
Design for Manufacturing	28
Design for Environment	28
Design for Safety	28
Final Design	29
Validation of Design	30

	2
Design Improvement	31
Appendix B: Manufacturing Processes	32
Appendix C: Original Test Hierarchy	34
Appendix D: Description of Data Analysis Methods	35
Appendix E: Methods for Determining Vessel Velocity	37

Motivation

Cross flow turbines (CFTs) are a promising mechanism for harnessing energy in wind and water (tidal, river, or ocean) currents. Their unique design can allow lower cost, simpler maintenance, and less entrapped debris than other turbine types [1]. Most CFT designs require a structure to support both the top and bottom of the turbine drive shaft. Vertical-axis CFTs are typically supported at the base by a lander, and incorporate guy lines or a frame to support the upper end of the turbine. These elements incur their own construction and maintenance costs, and add additional disturbances to the surrounding environment. By contrast, a cantilevered support structure may lower construction and maintenance costs and reduce the amount of space required for each turbine unit. Additionally, the large central shaft required to resist hydrodynamic thrust loads might double as a housing for system elements such as the generator and power storage banks. This report details a preliminary investigation of the performance of a series of large central turbine shaft sizes, to examine the effects of a cantilevered design large enough to support the turbine and house other system elements internally.

Method

Equipment

This experiment utilized resources from both the UW Applied Physics Laboratory (APL) and UW Marine Renewable Energy Laboratory. All testing was conducted aboard the APL Research Vessel, Russell Davis Light (R/V Light). R/V Light (shown in Figure 1) is a new vessel, only recently completed in August of 2018, and is built for testing field-scale hydrokinetic turbines and other marine technologies. The vessel has a large gantry at the bow on which turbines can be mounted and lowered into the water in front of the vessel, where there are minimal effects from the hull. As of March 2019, this system is still receiving its final touches.



Figure 1. Research Vessel Russell Davis Light, with a CFT mounted on the gantry.

The gantry is equipped with multiple mounting points, allowing up to two CFTs to be mounted and their interaction studied. When the gantry is complete it will incorporate a number of sensors, including:

- 6 axis load cell: Measures thrust, lateral, and vertical forces on the turbine, as well as associated torques
- Torque cell: Measures net torque drawn or produced by turbine
- Optical angular position sensor: Reports the azimuthal position of turbine
- Turbine motor angular velocity: Reports both command and actual angular velocity of the motor that drives the turbine
- Acoustic Doppler velocimeter: Measures the velocity of incoming flow
- GPS: Reports the latitude and longitude of the vessel
- Temperature sensor: Measures the water temperature of the incoming flow.

Figure 2a shows a schematic of the turbine system used. At the time of testing, only the torque cell and GPS were available for use in data collection. While generator motor speed could be specified, real time feedback on motor and shaft angular velocity was unavailable.

A custom “clamshell” fixture (Figure 2b) was used to simulate larger turbine central shaft sizes. The clamshell assembly implemented nesting concentric PVC shells at nominal outer diameters of 5.5”, 8.625”, 12.25”, and 16”, and allowed for quick adjustment of central shaft size while the vessel was underway. The design and manufacturing of this assembly are described in detail in Appendix A and Appendix B, respectively.

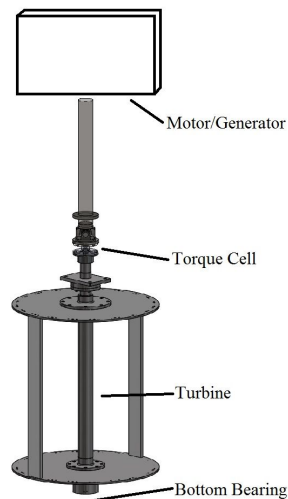


Figure 2a. Motor, torque cell, bearing, and cross-flow turbine arrangement



Figure 2b. Half of clamshell assembly installed on CFT shaft

Experimental Design

Table 1 provides a list of the parameters used in both experimental design and data analysis. These will be referenced throughout this paper.

Table 1: Parameters for analysis of cross-flow turbines

Symbol	Parameter
Q_h	Hydrodynamic torque
ω	Rotational velocity
ρ	Density
U_∞	Free-stream velocity
r	Turbine radius
A	Swept area
r_b	Shaft blockage ratio
λ	Tip speed ratio
C_p	Coefficient of performance
Re_c	Chord length Reynolds number

The swept area of the turbine is the product of the turbine's height and its diameter, given by

$$A = 2r * h . \quad (1)$$

For convenience, shaft blockage ratio, r_b , was defined as the ratio of the turbine's swept area to the shaft's projected area, given by

$$r_b = \frac{A_{shaft}}{A_{turbine}} = \frac{d_{shaft}}{2r} . \quad (2)$$

The tip speed ratio (or TSR), is the ratio of the blade speed to that of the free stream velocity, given by

$$\lambda = \frac{\omega r}{U_\infty} . \quad (3)$$

The coefficient of hydrodynamic performance, or C_p , is used to assess the power generation capabilities of the turbine, and is the ratio of the power generated or consumed by the turbine to that available in the free stream as

$$C_p = \frac{\omega Q_h}{\frac{1}{2} \rho A (U_\infty)^3} . \quad (4)$$

Lastly, the Reynolds number with respect to chord length (C), or Re_c , provides a measure of the ratio of inertial effects to viscous effects in a fluid flow, as

$$Re_c = \frac{U_\infty C}{\nu}. \quad (5)$$

Many parameters affect the performance of a cross flow turbine. Those that can be controlled on R/V Light are:

- Number of blades
- Blade preset pitch angle
- Blade chord length
- Tip speed ratio
- Free stream velocity (Reynolds number)
- Shaft size

The amount of testing time available to the project was unknown during early planning stages, so a hierarchy was devised ranking the importance of testing each variable. A full version of this hierarchy is given in Appendix C. Testing with a single blade was given top priority, for clarity when associating fluid dynamic events in a cycle with blade position. Unfortunately, there was only time for one day of testing, so this single-bladed series of tests are the primary data sets. A single two-bladed configuration was tested to see if the qualitative effects on the test system were similar to those of the one-bladed tests. The test plan specified a single blade chord length of 15 cm, 6° preset pitch, a range of tip speed ratios from 0 to 3, and all shaft geometries (including a stock shaft, bare of test assembly). This chord length and preset pitch angle were chosen to optimize performance based on previous research [2, 3]. An assembly mistake prior to testing resulted in a preset pitch angle of 0° being used. Final test parameters are given in Table 2.

Table 2. Experimental parameters for testing

<i>Shaft diameter</i>	3.5" (stock)	5.5"	8.625"	12.25"	16"
<i>Shaft blockage ratio (r_b)</i>	0.10	0.17	0.26	0.37	0.48
<i>Number of blades</i>	1				
<i>Blade chord</i>	15 cm				
<i>Preset pitch angle</i>	0° (6° intended)				
<i>TSR range</i>	0 - 3				
<i>TSR step size</i>	0.3				
<i>Nominal vessel speeds</i>	2 kts, 4 kts				

Reynolds Number Dependence

Changes in the Reynolds number with respect to chord length (Re_c) are associated with significant changes in turbine performance due to the Reynolds number dependence of boundary layer attachment. However, if Re_c is large enough, fluid dynamics change minimally with Reynolds number; this is commonly referred to as “Reynolds independence”. It is desirable to

perform tests under Reynolds independent conditions to ensure results are generalizable. For cross-flow turbines of 1 meter diameter, Reynolds independence has been shown to occur at Re_c greater than $2 * 10^5$ [4]. According to this standard, Reynolds independence is only achieved at 4 kts, where $Re_c = 2.2 * 10^5$, given a water temperature of 7.5 °C. However, the threshold for Reynolds independence may be different for turbines tested in open water rather than confined channels (e.g., flumes), and testing at two different vessel speeds can assess where this threshold might be.

Experimental Procedure

The experimental procedure was a five-step process as follows:

1. Assembly
 - a. Assemble turbine at dock
 - b. Assemble full clamshell at dock
 - c. Remove work platform under gantry
2. Achieve testing conditions
 - a. Lower gantry
 - b. Accelerate to nominal vessel speed
3. Perform test
 - a. Increase turbine rotational velocity while maintaining vessel speed to change TSR
 - b. Collect torque and GPS data for a TSR range of 0 to 3 with 0.3 increments, maintaining each TSR for 30 seconds
4. Remove shell
 - a. Stop the vessel
 - b. Raise gantry
 - c. Remove the outermost clamshell
 - d. Lower gantry
5. Repeat steps 3 and 4 until all configurations have been tested

Data Analysis

MATLAB was used for all data processing. This included a preliminary script to generate a C_p -TSR curve from data while the vessel was underway, which provided researchers a quick check to ensure proper system and sensor operation. Most data processing was performed after all tests were completed using scripts that calculated the coefficient of performance from torque data and plotted both C_p -TSR curves and phase-average C_p figures. Average velocity for the calculation of actual TSR and C_p was derived from the recorded GPS data. The methods used to process the data are described further in Appendix D.

In the absence of many sensors, several assumptions were made to simplify the analysis. Since the dynamic temperature sensor on R/V Light was not integrated at the time of testing, a constant water temperature of 7.5 °C was used to define the density and kinematic viscosity of water for all analyses [5]. As real time information on the rotational speed of the motor and turbine were not available, the rotational speed of the turbine was assumed to be as specified and constant for each 30 second TSR interval. Additionally, effects of bearing friction were neglected for this analysis, as this is generally negligible even at laboratory scale.

The following metrics were obtained in order to quantify the performance behavior of the turbine during the test:

- Cycle-average C_p : The average coefficient of performance over a single cycle (one turbine revolution)
- Time-average C_p : The average coefficient of performance over a single TSR interval
- Phase-average C_p : The coefficient of performance at each azimuthal blade position, averaged across multiple cycles at a single TSR.

Additionally, the interquartile range (IQR) of the cycle-average C_p values at each TSR was utilized to quantify variability in time-average performance over a single TSR interval.

Results

Test Equipment Performance

To provide context regarding the numerical results of the experiment, qualitative observations from the experiments are briefly described. Tests at a nominal vessel speed of 2 kts were executed smoothly. However, at a nominal vessel speed of 4 kts, significant vibrations of the vessel's gantry were observed. The magnitude of these vibrations increased with decreasing shaft size; in other words, as clamshells were removed from the assembly, the gantry vibrations became more intense. The largest gantry vibration magnitude occurred at a shaft angular velocity of roughly 111 rpm (or a generator rotational speed of 1785 rpm). These vibrations, combined with electrical issues on the vessel, limited the upper end of the testable TSR range at 4 kts to a nominal value of 2.4 for all turbine configurations that included the clamshell assembly, and 2.7 for the turbine configurations featuring only the stock shaft. The effects of this resonance on the data are not immediately apparent, but a fix for this problem is being developed.

Additionally, when the gantry was raised after some tests, the blade alignment pins in the top and bottom turbine plates were found to have shaken themselves loose to the point that some could be removed by hand. It is unclear how the failure of these alignment pins may have influenced

the results of this experiment, but, as the pins protruded into the flow, oppositional torque from drag on the pins would have increased, thereby reducing the measured hydrodynamic torque. Other than the resonant vibrations of the gantry and loosening of the alignment pins, all test equipment functioned without issue. Torques of up to 900 N-m (occurring for tests at 4 kts and smaller shaft sizes) were observed, only 100 N-m below the maximum allowable for the torque cell.

Performance vs Shaft Blockage Ratio

The data indicate a general decrease in turbine performance with increasing shaft size. As can be seen in Figure 3, for both vessel speeds tested, the best time-average C_p consistently decreased as the shaft blockage ratio increased, though the marginal decrease plateaued for larger shaft sizes. The TSRs at which these best C_p values occurred are given in Figure 4. It is worth noting that the optimal TSR for most shaft sizes was the highest TSR that was tested ($\lambda_{\text{nominal}} = 3$ for tests at 2 kts and $\lambda_{\text{nominal}} = 2.4$ for tests at 4 kts).

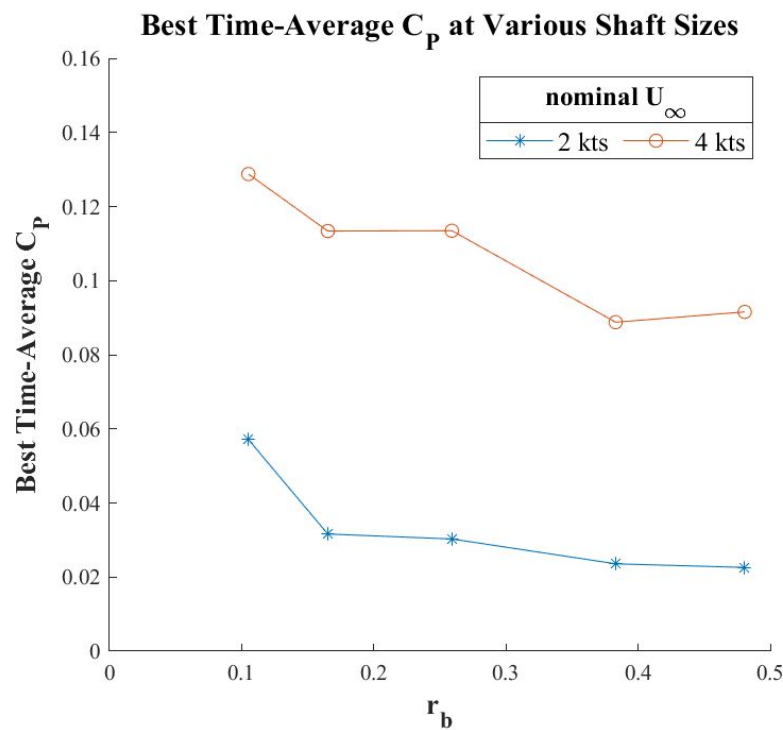


Figure 3. Time-average C_p at most efficient TSR, by shaft blockage ratio.

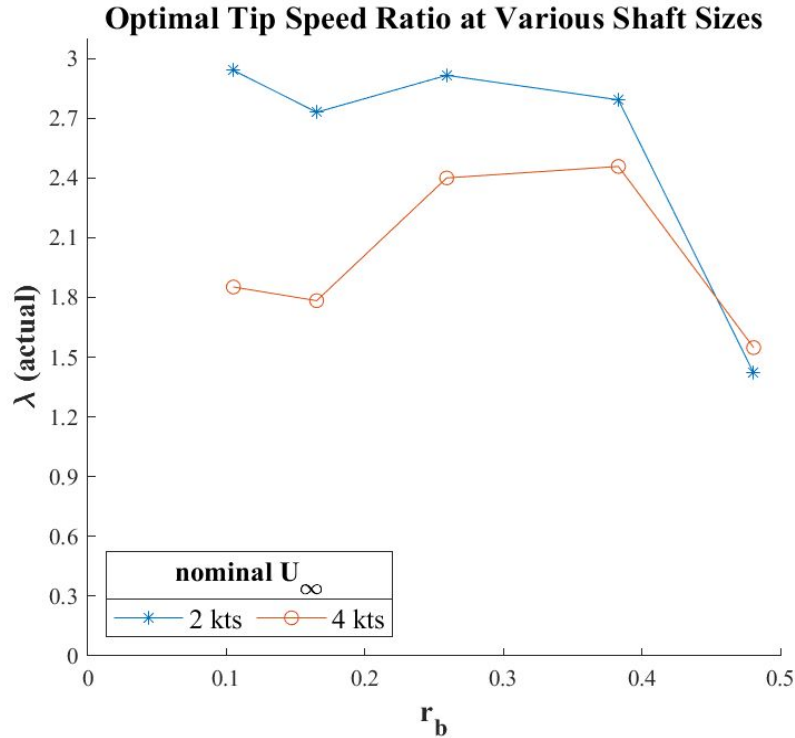


Figure 4. TSR providing highest average C_p by shaft blockage ratio

C_p vs TSR curves for different shaft sizes at TSRs above 1.0 are shown in Figures 5 and 6 for tests at 2 kts and 4 kts, respectively. For every turbine configuration, C_p values measured at a nominal vessel velocity of 4 kts were higher across the entire TSR range than those measured at a nominal vessel velocity of 2 kts. Additionally, smaller shaft sizes outperformed larger shaft sizes across the TSR range that was tested. This trend is more defined for tests at 2 kts. One notable exception to this behavior was seen at both vessel speeds. The shaft blockage ratio of 0.37 exhibited C_p values that were lower in almost every case than those for a shaft blockage ratio of 0.48. One possible explanation is that the outer clamshell profile corresponding to a shaft blockage ratio of 0.37 had more significant surface irregularities (such as eccentricity or raised edges) compared to the others, which would create more parasitic torque.

Additionally, it is likely that these C_p -TSR curves were not completely resolved for the TSR range tested. C_p -TSR curves from previous research involving two-bladed turbines show a performance peak around a TSR of 2, followed immediately by a steep drop-off in performance [2]. Both Figures 5 and 6 demonstrate generally increasing performance when the maximum TSR allowable for the operating platform is reached. Furthermore, most of the optimal TSRs given in Figure 4 were the maximum TSR tested. These results appear to indicate that the peak performance for a single-bladed turbine may be higher than the range that was tested. Future research should test higher TSRs in order to fully resolve the curve.

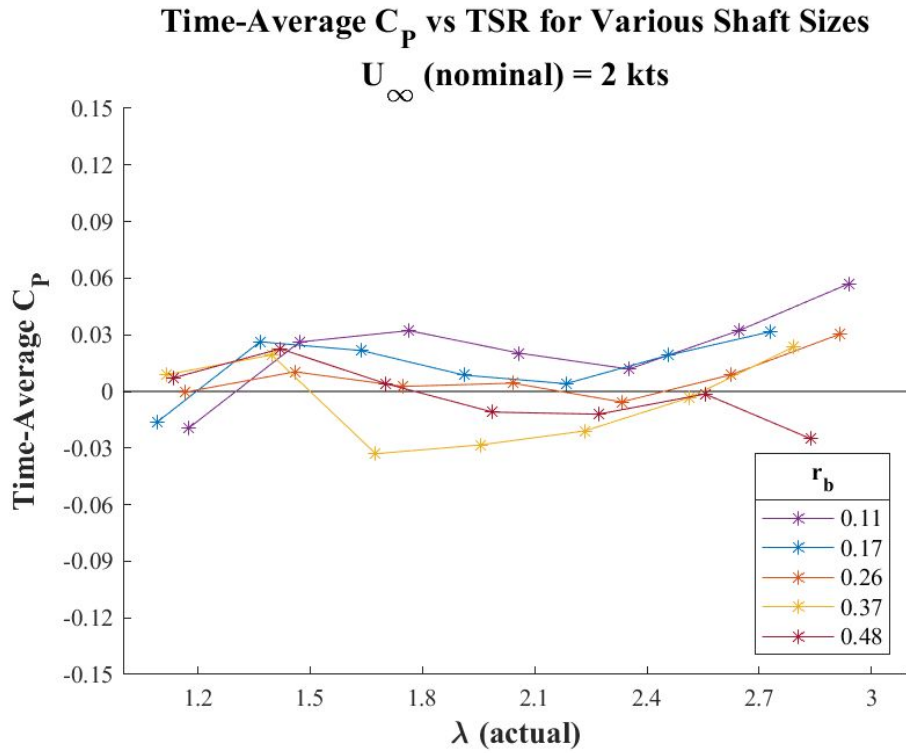


Figure 5. 2 kts performance curves

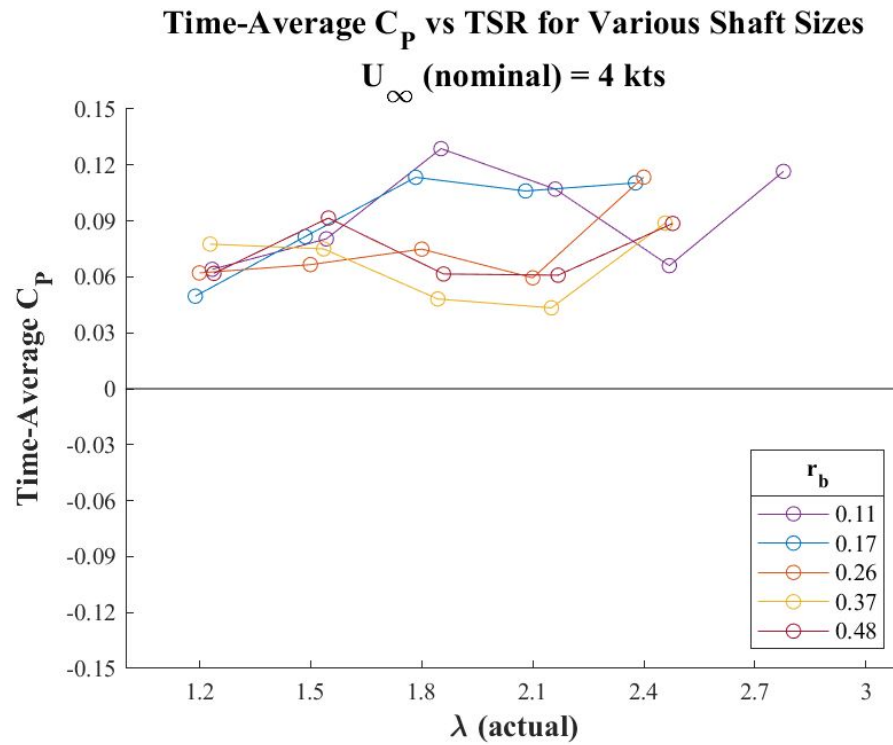


Figure 6. 4 kts performance curves

Reynolds Dependence

Previous research testing a one meter diameter turbine at Reynolds numbers greater than $2 * 10^5$ has exhibited Reynolds independence [4]. This experiment was conducted at Reynolds numbers of $Re_c = 1.1 * 10^5$ and $Re_c = 2.2 * 10^5$ for the 2 and 4 knot inflows, respectively. This would imply that results obtained at 4 kts inflows may be generalizable, while results at 2 kts are Reynolds dependent. However, further testing at higher Reynolds numbers is required to determine if this trend holds. As can be seen in Figures 7 and 8, 2 kts tests experienced almost half the peak performance that the 4 kts tests experienced across all shaft sizes.

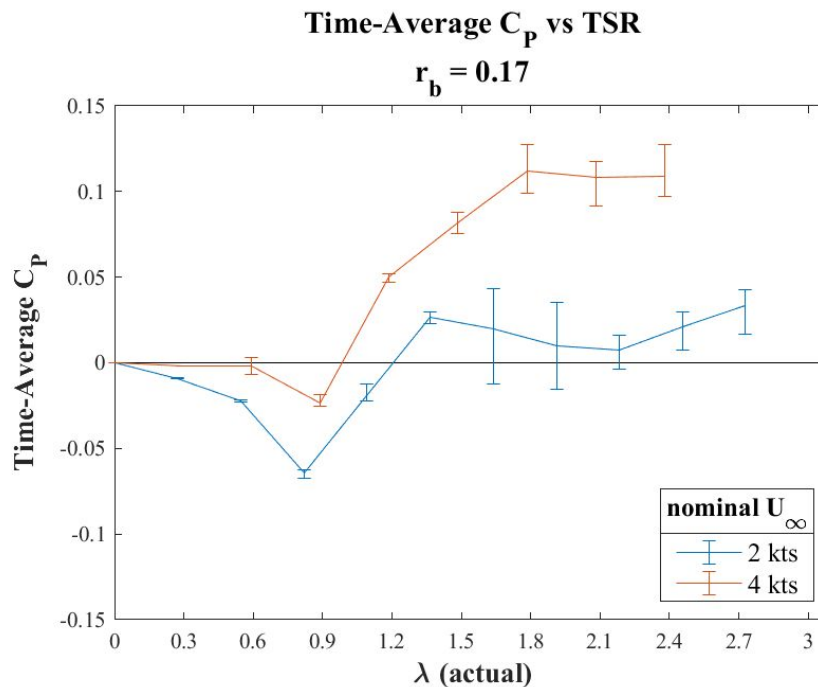


Figure 7. Comparison between C_p for 2 kts and 4 kts tests, 0.17 shaft blockage ratio

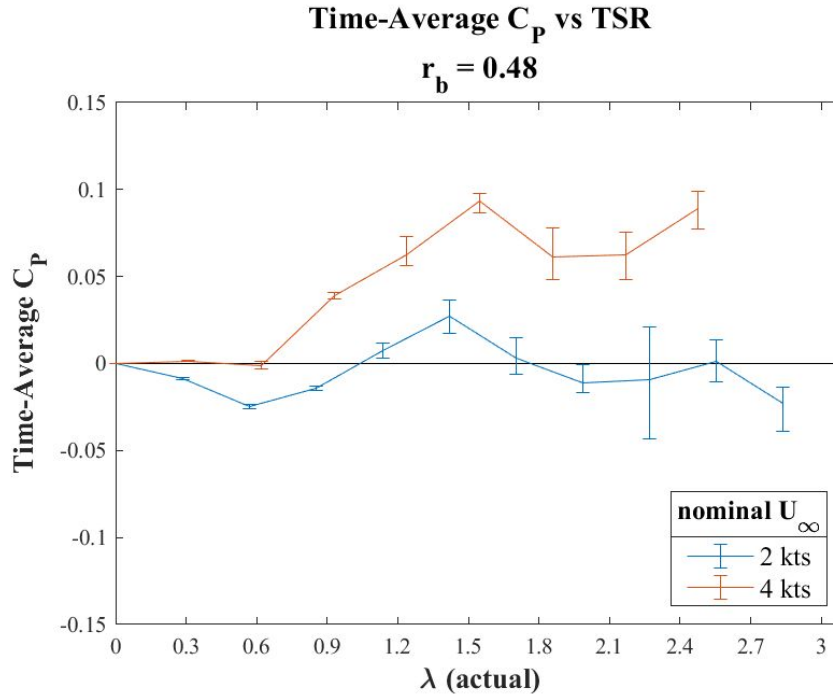


Figure 8. Comparison between C_p for 2 kts and 4 kts tests, 0.48 shaft blockage ratio

Phase Average Performance

While true phase-average results were not available due to the lack of a blade position sensor on the turbine on the day of testing, the analysis of individual cycle dynamics on the basis of maximum cycle torques provide some insight into how a larger shaft size impacts turbine performance. In the absence of a position sensor, a “working phase” of 0° is defined as the blade’s azimuthal position when maximum cycle torque occurred. However, as the location of the blade when maximum torque occurs may be a function of both TSR and shaft size, the blade’s azimuthal position at a working phase of 0° is likely not consistent across TSRs or shaft sizes. Regardless, the method utilized allows for comparison of what happens after the maximum torque occurs across tip speed ratios and configurations.

The phase average plots in Figures 9 and 10 show the changes in phase-average C_p at 2 kts within an individual cycle across the tested TSR range for the largest and smallest shaft blockage ratios tested. Maximum instantaneous C_p values were between 4 and 6. While instantaneous C_p values above the Betz limit have been observed in similar-scale research [6], values so much greater than 1.0 were unexpected, and need to be explored further, as the time-average C_p was within the expected range from tow tank tests of turbines of this size.

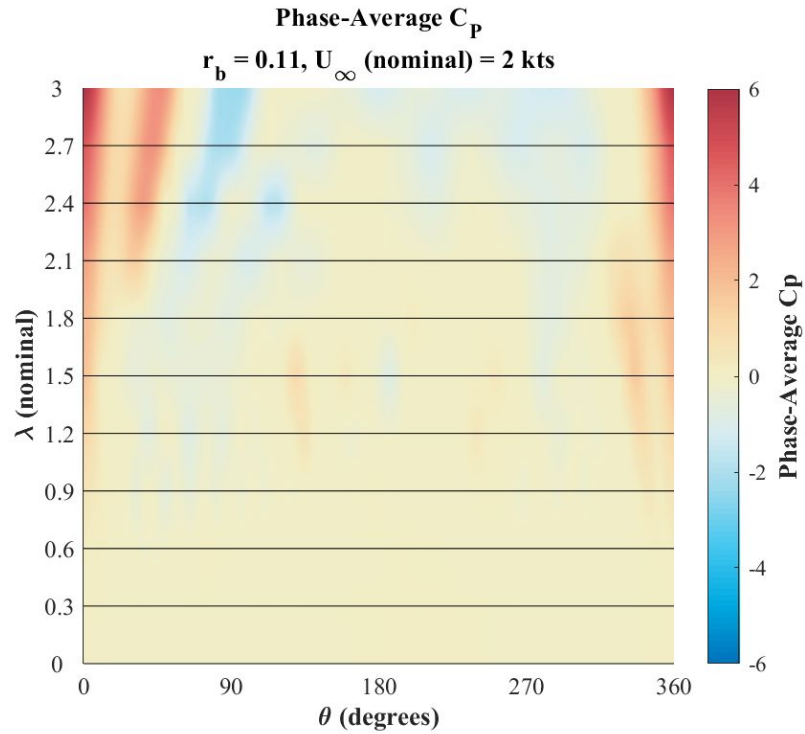


Figure 9. Phase-average C_p across angular turbine phase, shaft blockage ratio 0.11

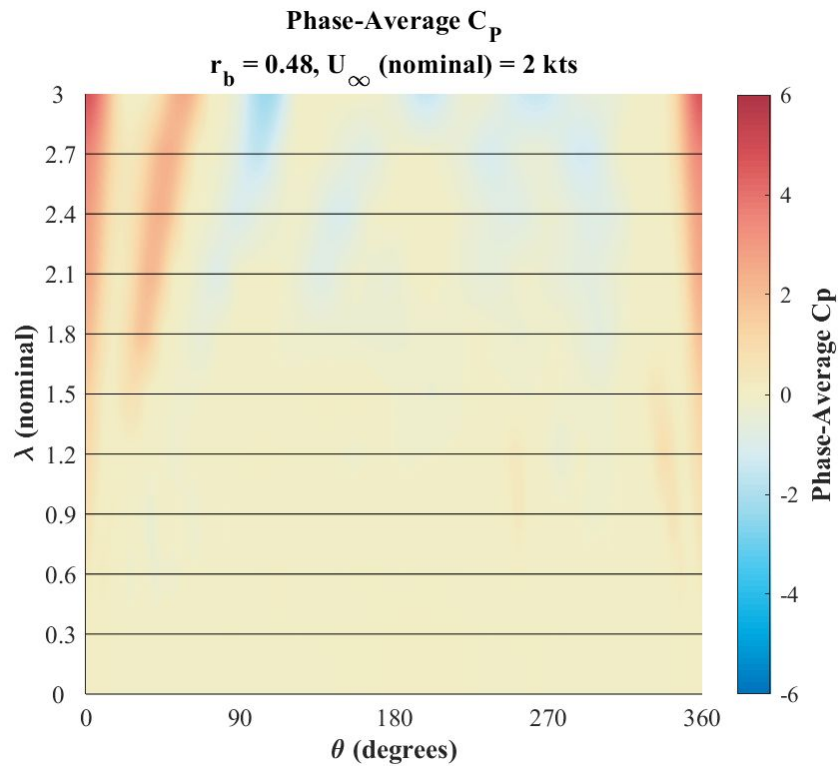


Figure 10. Phase-average C_p across angular turbine phase, shaft blockage ratio 0.48

In all 2 kts tests, the maximum C_p (corresponding to maximum cycle torque) is immediately followed by both a smaller, secondary C_p peak and the minimum cycle C_p . As the shaft blockage ratio increases, phases at which this secondary peak and minimum occur are shifted later in the cycle. Additionally, this secondary peak begins to manifest at lower TSRs when the shaft blockage ratio is larger. While firm conclusions cannot be drawn without a position sensor, these trends suggest that shaft size influences both the frequency of blade forcing and the azimuthal positions at which it occurs.

Performance Variations with Blade Count

Although alterations to turbine blade count were not included in the original design of the experiment, the performance of a two bladed turbine was briefly investigated to assess the effect of blade number on gantry vibrations that were observed at higher TSRs. Adding a second blade appeared to successfully reduce the magnitude of resonant vibrations observed at higher TSRs at 4 kts, and allowed for the full range of TSRs to be tested. As can be seen in Figures 11 and 12, and as expected [2], the two-bladed turbines performed significantly better, on average, than single-bladed turbines.

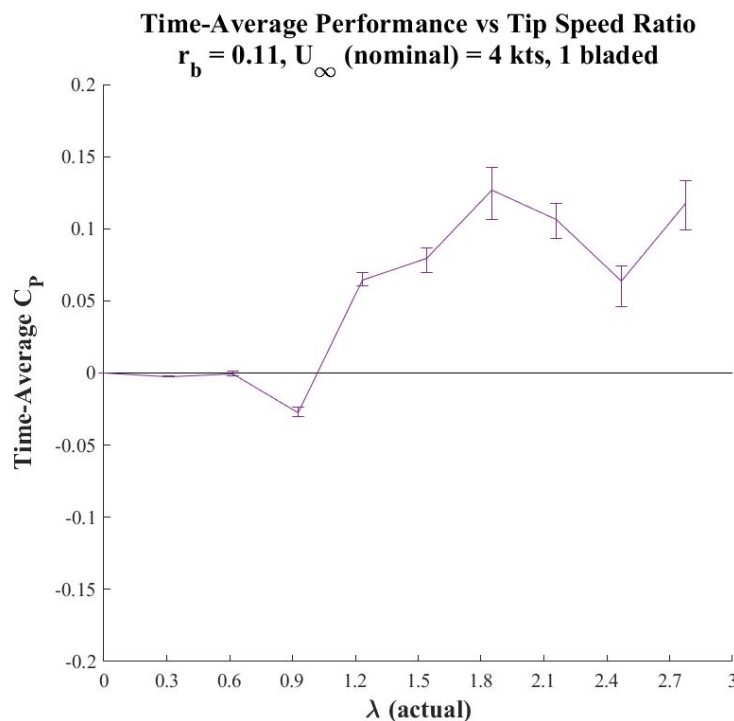


Figure 11. Performance of a 1 bladed turbine at $r_b = 0.11$ and 4 kts

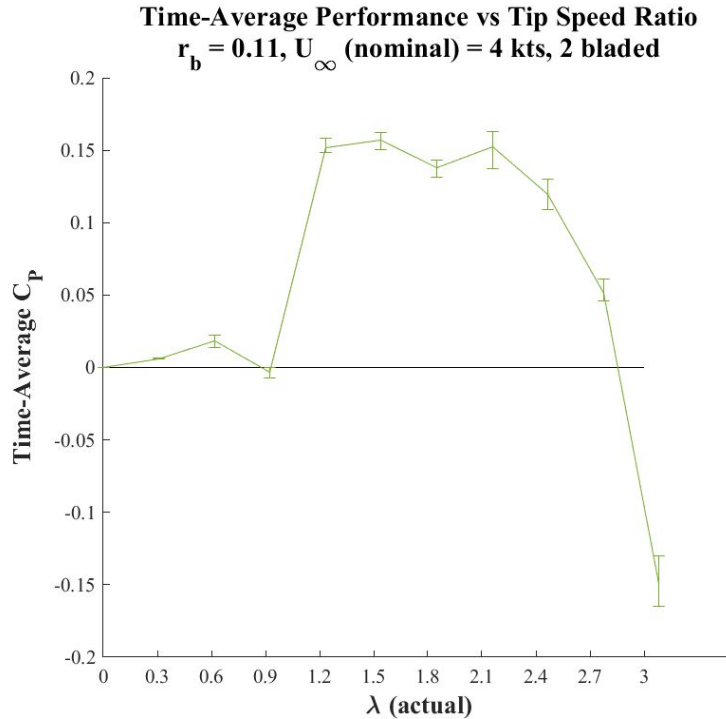


Figure 12. Performance of a 2 bladed turbine at $r_b = 0.11$ and 4 kts

Discussion

Sources of Error/Uncertainty

As this experiment was the first to be conducted aboard R/V Light, there are many contributors to error and uncertainty in these results. As mentioned previously, significant gantry vibrations occurred when testing the turbine at high tip speed ratios at a nominal vessel speed of 4 kts. The effect of these vibrations on torque readings is currently unknown, but may be quantified by continued characterization over the next few months.

Eccentricity in the PVC shells that were used to simulate larger shaft sizes may have also influenced these results. Irregularities in the shape of the schedule 40 PVC used in the clamshell assembly arose from residual stresses in the PVC that caused it to deform when cut lengthwise in half. Additionally, poor manufacturer tolerances led to variations from nominal size in the PVC as-received. This eccentricity was not quantified during testing, but it is estimated that there were variations in diameter of up to 10 mm in larger shell cross-sections. Future work involving the clamshell assembly should seek to quantify this eccentricity and potentially use an azimuthal position sensor to understand the intra-cycle impacts of these irregularities.

Variation in vessel speed from nominal values could have significantly impacted the results as well. GPS data were used to estimate actual vessel velocity, and the methods applied are described in Appendix E. While average vessel velocity over the course of an entire test could be estimated from GPS data, instantaneous velocity could not be obtained accurately. Further, small differences in average velocity propagate quickly through results. As can be seen in the equation for C_p (Equation 4), since the free stream velocity term, U_∞ , is cubed, a change of only 0.1 kts in vessel speed corresponds to a 5% change in calculated C_p value. Implementation of an acoustic Doppler velocimeter (ADV) should be prioritized in future experiments to alleviate this error.

As a working water temperature probe was not available on the day of test, a constant temperature was assumed for data analysis. A local water temperature of 7.5 °C, which was obtained from a King County data collection buoy in Lake Washington on the morning of the test, was used throughout all calculations [5]. Assuming a constant temperature neglects instantaneous changes in water properties, such as density and viscosity. A temperature probe should be used to quantify changes in water temperature in future tests.

Bearing losses due to turbine misalignment also contribute unquantified error to this data. These losses are expected to be quantified through additional characterization testing of the system in the near future.

Lastly, the data collected corresponds to a very small sample size. Testing was limited to one day on the water, with only one trial performed for each turbine configuration. Repeated data collection is recommended to solidify the conclusions drawn from these results.

Environmental Impact

Further commercialization of current energy-harvesting devices like CFTs may detrimentally affect marine fauna. There is potential for physical harm if animals enter the rotor-swept area. CFTs are intended to be used in regions where the high-speed flows can limit aquatic life's ability to react to obstructions in the water. CFTs tend to exhibit peak performance at relatively low tip-speed ratios, which inherently decreases the potential for aquatic life fatalities on impact. However, use of a cantilevered support and lander rather than an external frame decreases the solidity of the turbine, which may increase the chances of fish being physically harmed. As an example, the ORPC RivGen turbine in Igiugig, Alaska has operating during a period in which an estimated 2 million adult sockeye passed by the turbine with almost no interaction [7]. This indicates that the structural support may, in fact, have minimal impact on fish's avoidance.

In addition to the positive effects of the commercialization of CFTs in general, the simplicity of a cantilevered turbine should reduce greenhouse gas emissions over its life cycle by reducing the materials needed for manufacture, installation and maintenance. To maximize this potential gain, CFTs are proposed as an alternative to diesel generators for remote communities.

Societal Impact

Since a primary goal of the cantilevered structure design is to reduce the structures external to the turbine, it could increase the range of recreational and commercial activities that can be practiced near the turbine. Decreased construction and maintenance costs may lower the barrier to entry for small communities currently lacking adequate connectivity to the power grid, empowering reduced diesel generator use. Divers working to install and maintain cantilevered CFTs will benefit from fewer obstructions, removal of the dangers associated with high tension lines and large structures, and overall reduced underwater work.

There is potential for negative societal impact, however, such as increased likelihood of fish net entanglement due to the lack of a frame around the turbine. Turbines deployed on landers may also be easier to deploy in areas previously considered unsuitable for marine energy development, possibly reducing the area available for recreation and fishing. While previous research has established ample societal interest in the development of marine renewable energy, these concerns can all contribute to negative public perception.

Economic Analysis

The economic feasibility of a large central shaft turbine has many factors to account for beside the capital cost associated with the structure itself. These include any efficiency lost or gained over the turbine's lifetime, the cost of installation and decommissioning for the structure, any associated maintenance, and change in lander needs for each design. Research by the Strategic Initiative for Ocean Energy (SI OCEAN) found that for tidal energy sources, the installation, maintenance, and mooring required are the largest costs over the life of the turbine [8].

The costs that are easily compared are the raw material cost of a large central shaft architecture, an aluminum frame architecture, and a guy-wire architecture. In a raw material cost comparison, the frame and large central shaft architectures were found to have comparable capital cost. While the guy-wire architecture was found to have a lower material cost, additional installation and maintenance costs are expected to outweigh these benefits. In addition, the guy-wire architecture creates a higher likelihood of fishing vessel entanglement. The operating costs associated with accidents with fishing vessels are unknown and should be a point of future work.

Risk and Liability

To reduce risk to researchers and property, the test rig was designed to be as safe to operate as possible. Researchers sought to reduce the frequency that the gantry must be raised and lowered, weight of components, time, and number of tools necessary to switch from one geometry to another. The nested clamshell concept unites these principles by allowing all shaft sizes to be assembled and aligned while the vessel is docked, and with the work platform secured underneath. Removing each shaft only requires removing screws with a single driver bit and handing components off to another team member on deck. All of these operations can be performed from the catwalk and with appropriate PPE (hard hat, life vest, proper footwear). Reducing the possibility of dropping components was also considered; plain steel fasteners and magnetic driver bits were used, as well as eye bolts tied to line that allow baffles and shells to be secured to each other and reduce the possibility that a single item can be dropped in the water.

Ethics

The largest ethical issue with the data presented in this report is the potential to make decisions based on trends that need further testing to confirm. Over- or underestimating the ability of the turbine to perform with large central shafts could lead to misled design and construction, which would hinder the growth of tidal energy development if public funded research results in poor turbine performance. Identifying future work was a large part of this study. It is again noted that the small sample size and other sources of error detailed above must be considered in any-decision making process.

Conclusion

This preliminary experiment demonstrates the viability of large shaft CFTs for tidal applications, especially in high-velocity flows. Results show decreasing performance with increasing shaft size. The best time-average C_p drops 30% between 0.11 and 0.47 shaft blockage ratios at inflow velocities of 4 kts, but drops 50% between the same shaft blockage range for 2 kts inflows. Reynolds independence is not observed between 2 kts and 4 kts tests. Phase average results suggest that shaft size influences both the frequency of blade forcing and the azimuthal positions at which it occurs. Further testing with azimuthal position sensing, active temperature monitoring, and inflow velocity measurement via ADV should be performed to confirm these findings. Future tests should explore 6° preset pitch and two bladed configurations, as this has been identified as a higher performing configuration in prior study. Future one-bladed tests should be performed at higher TSRs in order to more fully resolve the C_p -TSR curve. Additionally, future tests require a solution to limit gantry resonance, such as increasing gantry

rigidity or adding damping mechanisms. Finally, profile eccentricity should be quantified before further testing is performed with the clamshell test assembly.

References

- [1] Ferrer, E. and Montlaur, A. “CFD for Wind and Tidal Offshore Turbines.” Springer, 2015.
- [2] B. Strom, B. Polagye, and S. Brunton, “Hydrodynamic Optimization of Cross-Flow Turbines with Large Chord to Radius Ratios,” *Proceedings of 3rd Marine Energy Technology Symposium*, Washington, DC, 2015.
- [3] B. Strom, B. Polagye, and S. Brunton, “Consequences of Preset Pitch Angle on Cross-Flow Turbine Hydrodynamics,” *11th European Wave and Tidal Energy Conference*, Nantes, France, 2015.
- [4] P. Bachant, M. Wosnik, “Effects of reynolds number on the energy conversion and near-wake dynamics of a high solidity vertical-axis cross-flow turbine”, *Energies* 9, 73 (2016).
- [5] King County, “Lake buoy data, Historical Temperature”, 2019. [Online]. Available: <https://green2.kingcounty.gov/lake-buoy/HistoricalTemperature.aspx>. [Accessed Mar. 20, 2019].
- [6] B. Strom, “Cross-Flow Turbine Fluid Mechanics: Experimental Optimization and Analysis,” D. S. thesis, University of Washington, Seattle, WA, 2019.
- [7] S. Kist, “ORPC RivGen® Power System Delivers Power to Remote Alaskan Village Grid Affordable, Clean Energy for Islanded Communities Now a Reality,” *Ocean Renewable Power Company*, July 30, 2015. [Online Serial]. Available: <http://www.orpc.co/uploads/news/orpc%20rivgen%20power%20system%20delivers%20power%20to%20remote%20alaskan%20village%20grid%20%20july%2030,%202015-2015730143.pdf> [Accessed Mar. 20, 2019].
- [8] “Ocean Energy: Cost of Energy Reduction Opportunities,” *Intelligent Energy Europe*, May, 2013. [Online Serial]. Available: https://energiatalgud.ee/img_auth.php/1/10/SI_OCEAN._Ocean_Energy_-_Cost_of_Energy_and_Cost_Reduction._2013.pdf [Accessed Mar. 20, 2019].
- [9] P. Gerhart, A. Gerhart, J. Hochstein, “Munson, Young, and Okiishi’s Fundamentals of Fluid Mechanics 8th Edition,” Wiley, 2016
- [10] Smits, A.J. “A Physical Introduction to Fluid Mechanics, 2nd Edition”, 2018.

- [11] “Mechanical Properties Table”, n.d. [Online]. Available:
http://atc.sjf.stuba.sk/files/mechanika_vms_ADAMS/Contact_Table.pdf [Accessed
Mar. 20, 2019].

Appendix A: Design

The initial project design specification required a system capable of interfacing with existing turbines. The purpose was to augment the profile of the central shaft, simulating the hydrodynamic effects of a large shaft such as would be required for a cantilevered (single-shear) turbine axle support assembly as opposed to a guy-line or frame-secured double-shear assembly.

Needs:

- Interfaces with existing turbines
- May be manufactured and tested within one quarter
 - Parts sourceable in less than two weeks
 - Limited modification required of off-the-shelf parts

Wants:

- Quick assembly/disassembly
- Safe assembly/disassembly over water
- Maximum tests within time on water (daily boat cost, possible test days)
- Durability (may be used for future testing by APL)

Concept Generation

A morphological chart was used to generate design ideas and narrow down to a workable solution. Table A.1 depicts the central functional statements of the turbine shaft design problem, as well as various concepts generated to address them. The solutions chosen are highlighted in green.

Table A.1 Morphological Chart

Functional Statement	Concept 1	Concept 2	Concept 3	Concept 4
<i>Mates to 3.5" shaft</i>	Compressed rubber	Set screws	Magnets	Pins
<i>May be reconfigured quickly in the field</i>	Clamshell	Universal mount	Telescoping supports	
<i>Resists deformation due to hydrodynamic effects</i>	Rigid construction (steel/al, fiberglass)	Flexible construction w/ reinforcement (baffles/gussets)		
<i>Minimal parasitic drag</i>	Recessed fixtures	Wax smoothing of butts, fixtures, interfaces	Tape smoothing	Gaskets/rubber at interfaces
<i>Locates profile radially</i>	Spokes	Thin discs		
Non-Functional Concerns				
<i>Manufacturability</i>	PVC profiles (potentially size limited)	Laser cutting reinforcements	Waterjet cutting reinforcements	
<i>Ease of assembly/disassembly</i>	Reusable/quick smoothing method	If clamshell, assembly holds together when outer is removed		

Friction from compressed rubber was selected for a simple, non-marring interface between the central shaft and the experimental system. To enable quick reconfiguration in the field, a “clamshell” system was chosen. This system would allow all shaft sizes to be installed at once, then removed layer by layer during testing. Spacers were chosen to maintain circularity of the shaft profiles, allowing the use of lighter and more easily manufacturable profile materials (as opposed to metallic or composite profiles). Recessed fasteners and tape-smoothing of transverse profile interfaces were selected to limit drag. Selected materials and associated reasoning are given in Table A.2.

Materials Selection

<i>Table A.2 Material Selection and Rationale</i>		
Part	Material	Primary Deciding Factors
Profiles	Sch. 40 PVC	<ul style="list-style-type: none"> ● Readily available in diameters of interest between 4” and 16” ● Inexpensive ● Sufficiently rigid (see <i>PVC Beam Bending</i>) ● Easy to cut (to length and in half)
Spacers	$\frac{3}{4}$ ” Delrin	<ul style="list-style-type: none"> ● Machineable ● Durable
Spacer-Shaft interface	1/16” Nitrile, polyester backing	<ul style="list-style-type: none"> ● Sufficient friction to resist expected torques (see <i>Rubber Compression</i>)
Fasteners	$\frac{1}{4}$ ”-20 Steel	<ul style="list-style-type: none"> ● Consistency in manufacturing ● Attraction to magnetic tools

Design Calculations

Several failure modes were explored computationally to confirm design and material selection choices. These included (1) the possibility of the profiles deforming or fracturing under the thrust loads experienced during testing, and (2) the potential for the experimental system to slip on the turbine shaft due to torque loads.

1. PVC beam bending

Finite element analysis (FEA) was employed to assess the susceptibility of schedule 40 PVC to deformation under hydrodynamic loading. Worst case drag forces at a free stream velocity of 3.5 m/s, which was higher than the largest nominal velocity in this experiment by 1.5 m/s, were estimated for each clamshell using drag coefficients obtained from a chart describing drag

coefficients of cylinder (Figure A.1). To simplify the model, the clamshell assembly was assumed to not be rotating.

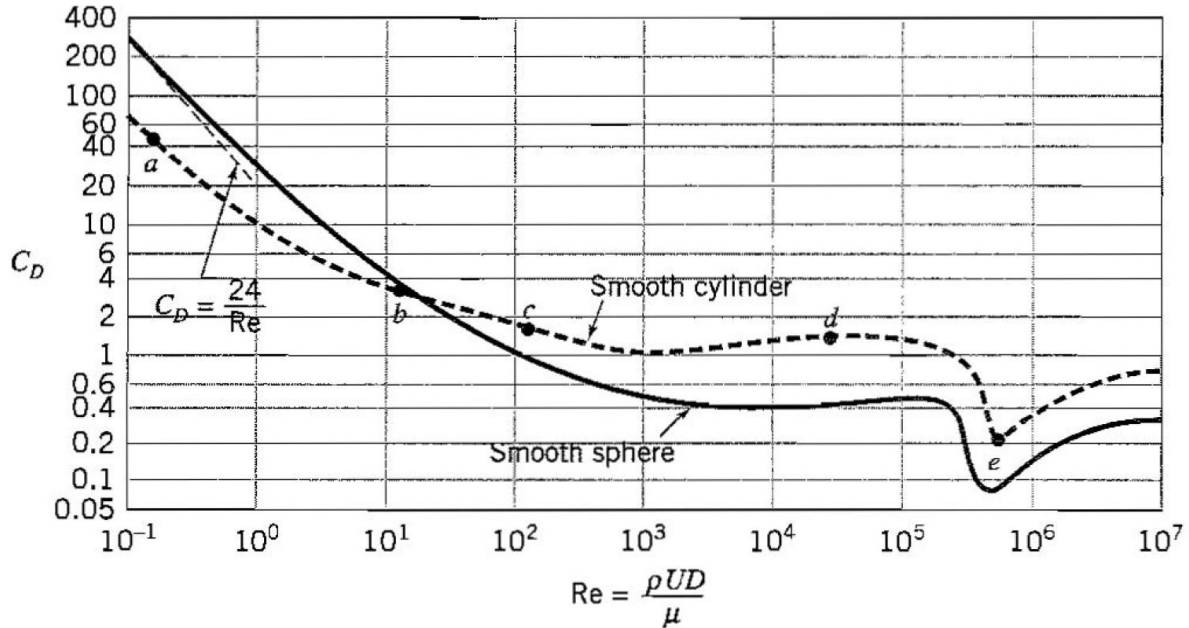


Figure A.1. Coefficient of drag on a smooth cylinder as a function of Reynolds number [9]

To find the drag coefficient, the Reynolds number with respect to diameter was evaluated for each shaft size. A water temperature of 20 °C was assumed for this analysis, which gives a density of 1025 kg/m³ and a dynamic viscosity of 1.14 * 10⁻³ N*s/m². Using Equation 5 (and replacing chord length with actual shaft diameter as the characteristic dimension), the Reynolds number with respect to diameter for each shaft size is calculated.

$$Re_D = \frac{U_\infty C}{\nu} = \frac{\rho U_\infty D}{\mu}$$

$$Re_{d, 5.5"} = \frac{1025 \text{ kg/m}^3 * 3.5 \text{ m/s} * 5.5 \text{ in}}{0.00114 \text{ N*s/m}^2} * \frac{0.0254 \text{ m}}{1 \text{ in}} = 4.40 * 10^5$$

$$Re_{d, 8.625"} = \frac{1025 \text{ kg/m}^3 * 3.5 \text{ m/s} * 8.625 \text{ in}}{0.00114 \text{ N*s/m}^2} * \frac{0.0254 \text{ m}}{1 \text{ in}} = 6.89 * 10^5$$

$$Re_{d, 12.25"} = \frac{1025 \text{ kg/m}^3 * 3.5 \text{ m/s} * 12.25 \text{ in}}{0.00114 \text{ N*s/m}^2} * \frac{0.0254 \text{ m}}{1 \text{ in}} = 9.79 * 10^5$$

$$Re_{d, 16"} = \frac{1025 \text{ kg/m}^3 * 3.5 \text{ m/s} * 16 \text{ in}}{0.00114 \text{ N*s/m}^2} * \frac{0.0254 \text{ m}}{1 \text{ in}} = 1.28 * 10^6$$

Referring back to the drag coefficient chart, it can be seen that this range of Reynolds numbers roughly corresponds to the valley between Reynolds numbers between 10⁵ and 10⁶. To avoid this valley and obtain a worst-case scenario corresponding to higher loading on the clamshells, higher drag coefficients than those corresponding to the calculated Reynolds numbers are used. In this

case, a drag coefficient of 1.5 was assumed for all clamshell sizes. The total drag force on each clamshell is then evaluated.

$$F_D = \frac{1}{2} \rho A C_D U_\infty^2$$

$$F_{D, 5.5"} = \frac{1}{2} * 1025 \text{ kg/m}^3 * (5.5 \text{ in} * 46 \text{ in}) * \frac{(0.0254 \text{ m})^2}{1 \text{ in}^2} * 1.5 * (3.5 \text{ m/s})^2 = 1537 \text{ N}$$

$$F_{D, 8.625"} = \frac{1}{2} * 1025 \text{ kg/m}^3 * (8.625 \text{ in} * 46 \text{ in}) * \frac{(0.0254 \text{ m})^2}{1 \text{ in}^2} * 1.5 * (3.5 \text{ m/s})^2 = 2411 \text{ N}$$

$$F_{D, 12.25"} = \frac{1}{2} * 1025 \text{ kg/m}^3 * (12.25 \text{ in} * 46 \text{ in}) * \frac{(0.0254 \text{ m})^2}{1 \text{ in}^2} * 1.5 * (3.5 \text{ m/s})^2 = 3424 \text{ N}$$

$$F_{D, 16"} = \frac{1}{2} * 1025 \text{ kg/m}^3 * (16 \text{ in} * 46 \text{ in}) * \frac{(0.0254 \text{ m})^2}{1 \text{ in}^2} * 1.5 * (3.5 \text{ m/s})^2 = 4472 \text{ N}$$

ANSYS workbench was used to simulate the clamshell system. One half of each clamshell size and corresponding delrin spacers were modeled in SolidWorks. Meshing settings that discretized the models into roughly 500,000 elements (the limit for the provided ANSYS license) were used.

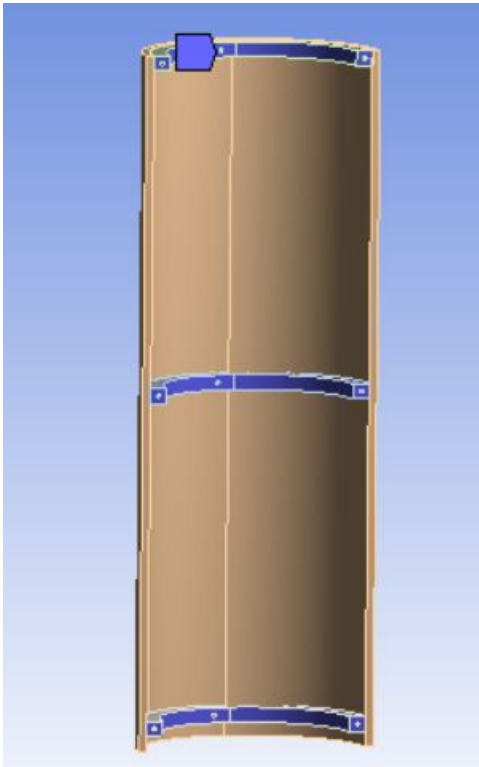


Figure A.2. The faces of the delrin spacers that were specified as fixed supports (highlighted in purple).

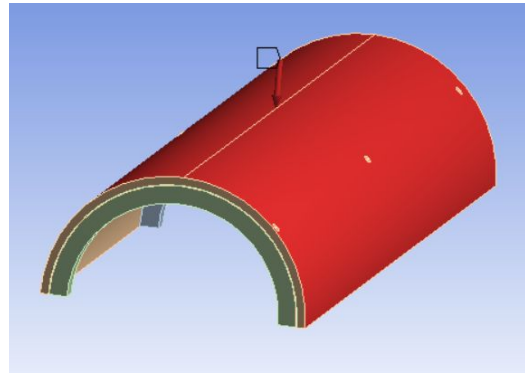


Figure A.3. (Top): The distributed drag force applied in both loading models.

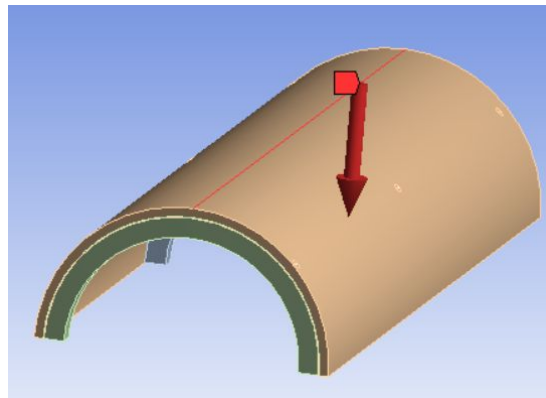


Figure A.4. (Bottom): The concentrated force applied in the non-uniform loading model.

The inside faces of the delrin spacers, which, when assembled, would be supported by either the stock shaft or the previous shell, were treated as fixed boundary conditions (shown in Figure A.2). Two loading models were investigated. In the first, most simple model, the entire drag force was assumed to be distributed uniformly in the direction of flow across the half-clamshell. This is shown in Figure A.3. However, noting that the part of the clamshell closest to the inflow is likely to receive the brunt of the drag force, a second model with non-uniform loading was investigated. In this model, $\frac{3}{4}$ of the total magnitude of the drag force is applied to the very front edge of the half-clamshell (as shown in Figure A.4), and the remaining $\frac{1}{4}$ of the force is applied uniformly across the surface in the direction of flow (as shown in Figure A.3).

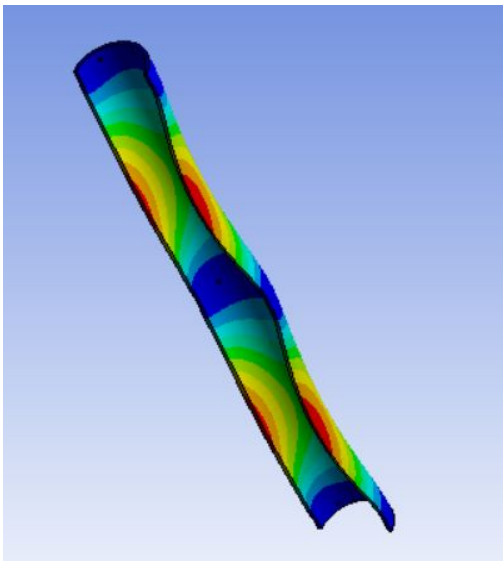


Figure A.5. Deformation of the 5.5" PVC clamshell under the uniform loading model. Larger deformations are shown as red.

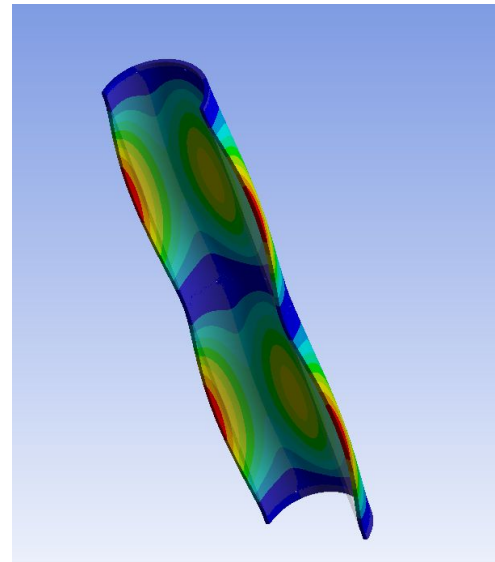


Figure A.6. Deformation of the 8.625" PVC clamshell under the non-uniform loading model. Larger deformations are shown as red.

Static structural ANSYS simulations resulted in very small deformations to schedule 40 PVC clamshells. The 5.5" PVC (Figure A.5) experienced the largest deformation under the uniform loading model, at 0.492 mm. The 8.625" PVC (Figure A.6) experienced the largest deformation under the non-uniform loading model, at 0.469 mm. Maximum deformations were shown to occur at the edges of the half-clamshells.

As these small deformations resulted from overestimations of the drag forces that the clamshells would experience, schedule 40 PVC was deemed a safe material choice. The large deformation at the clamshell edges prompted consideration of latches or tape to support these edges. While the model applied does offer a fair approximation of the load bearing capabilities of the PVC, it

is worthy of note that this configuration does not take into account the displacement of the PVC due to residual stresses that were encountered when the pipes were cut in half lengthwise.

2. Rubber compression

To calculate nitrile rubber compression required to resist movement due to drag forces on the experimental system, the largest profile was modeled as a flat plate moving through water at $\lambda = 3$ and 5 knots inflow velocity (a much higher inflow than expected during testing). The Reynolds number was calculated to determine flow regime, using the circumference of the shaft as the characteristic length:

$$Re_L = \frac{U_\infty * L}{\nu} = 5325 < 500,000 \rightarrow \text{laminar}$$

A laminar drag coefficient equation [10] was used to solve for force on the shaft, which was then converted to torque.

$$C_F = \frac{1.46}{\sqrt{Re_L}} = .0200$$

$$F = \frac{1}{2} \rho C_F (U_\infty)^2 LW = 211 \text{ N}$$

$$\tau_{hydro} = N * m = 42.83 \text{ N * m}$$

The force at the central shaft required to supply this torque was calculated, along with the area of the contact patch. The spring constant of 1/16" nitrile rubber was calculated, and a static coefficient of friction of .63 [11] was used to find the percent compression of nitrile to supply the required torque.

$$\tau_{hydro} = \tau_{friction}$$

$$F_{friction} = \frac{\tau_{friction}}{(D_{shaft}/2)} = \frac{42.83 \text{ N*m}}{(0.0889 \text{ m}/2)} = 963 \text{ N}$$

$$F_{compressive} = \frac{F_{friction}}{C_f} = \frac{963}{.63} = 1530 \text{ N} = 343 \text{ lbf}$$

$$A = 3(.75 \text{ in})(2 * \pi * \frac{3.5 \text{ in}}{2}) = 24.7 \text{ in}^2$$

$$k = \frac{AE}{L} = \frac{(24.7 \text{ in}^2)(435 \text{ psi})}{1/16 \text{ in}} = 17.2e4 \text{ lb/in}$$

$$F = kx \rightarrow x = \frac{F_{compressive}}{k} = \frac{343 \text{ lbf}}{17.2e4 \text{ lb/in}} = .00199 \text{ in compression}$$

$$\frac{.00199 \text{ in}}{\frac{1}{16} \text{ in}} (100) = 3.2\% \text{ compression of nitrile}$$

For a factor of safety of ~6, 20% compression was chosen for the nitrile. This defined the size of the gap between the innermost spacers and the central shaft.

Design for Manufacturing

Due to time constraints on this project, limiting manufacturing time was a design priority. This informed:

- *Material selection.*
 - Delrin was appealing for its easy machinability. All spacers could be waterjet from a single sheet. Delrin could also be drilled and tapped quickly and with minimal damage to associated tools.
 - PVC was appealing for its ease of cutting and drilling.
- *Consistency in repeated parts.* Recognizing that there were 24 individual spacers requiring machining post-waterjet, consistent datums were used to define feature locations. This allowed for the rapid interchange of parts without modifying mill axes.
- *Limited fastener types.* In order to limit tool changes and mistakes, ¼-20 hardware was used throughout the assembly.

Design for Environment

Steps were taken to limit the possibility of contaminating the testing grounds with parts of the test assembly. These included:

- The use of plain steel fasteners and magnetic drivers to limit dropped bolts.
- The use of eye bolts and string to harness spacers during disassembly, as a failsafe against accidentally dropping delrin into the lake.
- Active monitoring of tape used to smooth edges on the test assembly. Initially a vinyl tape was used for smoothing, but during an initial test that tape was witnessed peeling off of the assembly. The gantry was raised, all vinyl tape removed, and clear packing tape installed. Finding that this tape better withstood the forces present during testing, clear packing tape was henceforth used for all testing.

Design for Safety

Due to factors inherent to testing on a boat and interacting with heavy machinery, safety was a central focus throughout the design process. This included:

- *Material selection.* While the team was tempted by the rigidity and durability of steel or aluminum profiles, the weight of these profiles would have imposed a safety risk on those tasked with wrestling them around on the bow of the vessel. This inclined the team toward lighter-weight materials such as PVC.
- *Reconfiguration method.* Due to limited/costly vessel time, it was desirable that the system be quickly reconfigurable on the water. This informed the clamshell design and model of a) full assembly on the dock prior to the test date followed by b) rapid, layer by

layer disassembly on the vessel, requiring little time/tooling and thus sufficiently safe to be performed without returning to dock.

A Design for Safety focus expanded beyond the physical design of the test assembly and into the methods and operating procedures of testing itself. This included:

- Personal Protective Equipment (PPE):
 - Life preservers worn by personnel working on the bow of the vessel.
 - Hard hats worn by personnel working with tools in and around the gantry system, as well as all personnel engaged in operating the gantry.
- Standard Operating Procedures (SOPs):
 - Verbal or hand signals from all personnel on the bow of the vessel required before operating the gantry

Final Design

While PVC is available in even-numbered outer diameters up to 16 inches, 5, 8, 12, and 16 inch nominal sizes of PVC were selected to provide a reasonable range of diameters while limiting testing. Delrin spacers (Figure A.7) were designed to mate to the central turbine shaft and fix each PVC profile layer relative to the next. Spacers employed fasteners to set height and radial alignment, as well as to mate with the spacer opposite. PVC profiles were designed to be held to the spacers via two screws at each spacer.

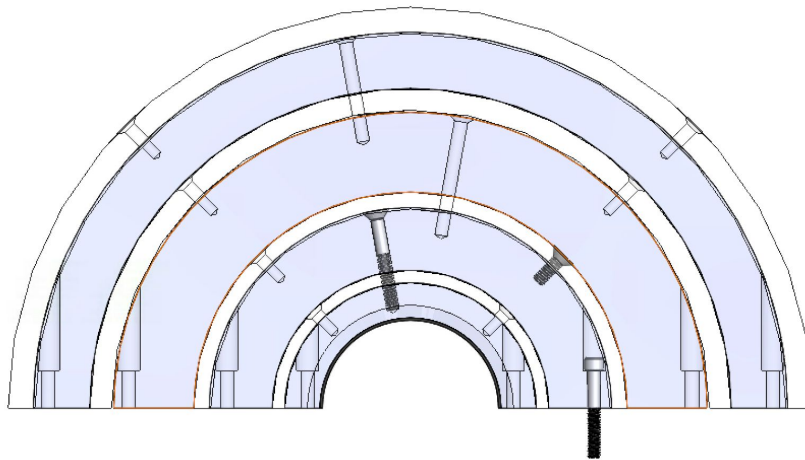


Figure A.7. Spacers (shaded), profiles (white), bores and example fasteners.

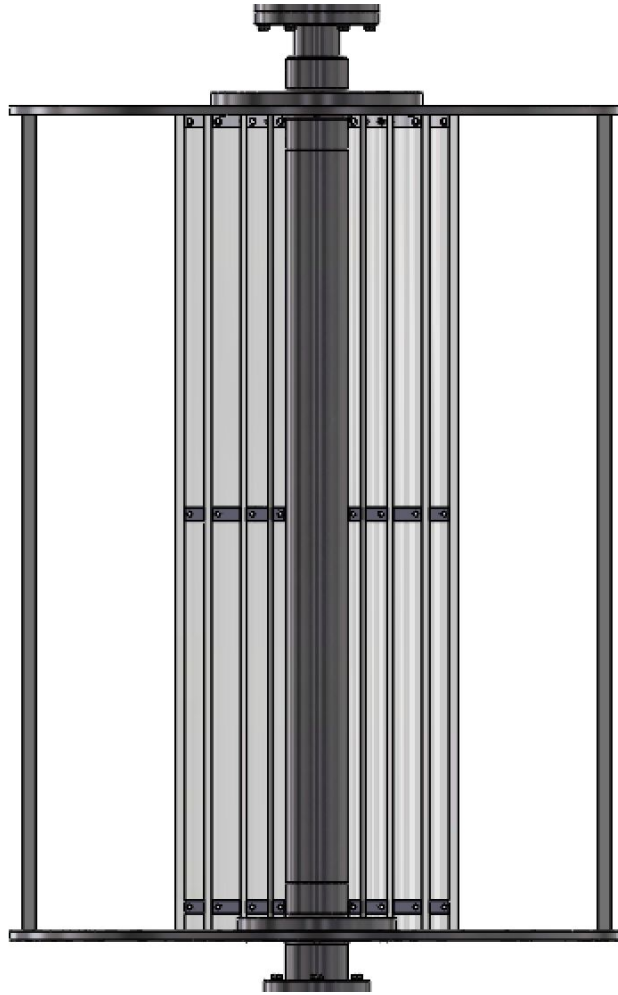


Figure A.8. Test Assembly on turbine shaft. Cylindricity of the profiles is maintained by spacers at both extremes and the center of the turbine shaft.

Validation of Design

Pre-testing design validation began by building the system up on a turbine installed on the gantry on R/V Russell Davis Light. Successful assembly was followed by preparation to spin the turbine in air via the control system. Turbine blades were removed. To track whether the test assembly spun separately from the turbine, both test assembly and turbine were marked. After spinning the turbine in air over 150 rpm, no damage and no clocking were observed.

The gantry was then lowered into the water, submerging the turbine and test assembly. Again the turbine was spun up to 156 rpm. Upon removal, no damage and no clocking were observed. Torque readings were around 55 N*m, 30% higher than estimated in the *Rubber Compression* analysis. This difference likely comes from parasitic drag due to eccentricity, taped joints, and fastener heads being spun through the water. The system was judged to work sufficiently well to begin testing.

Variability in parasitic drag between profile sizes is the main unquantified source of error that may influence measurements taken using this design. Due to residual stresses in the PVC profiles, each clamshell tends to spring toward a smaller diameter around its cylindrical axis; this effect is more pronounced for the larger profiles. While spacers maintain circularity at the top, bottom, and middle of the shaft, the unsupported $\frac{1}{4}$ and $\frac{3}{4}$ locations on the shaft exhibit eccentricity in the 2-5 millimeter range (this eccentricity has not been measured). The excess drag resulting from eccentricity, as well as from possible deformation during assembly due to residual stresses and the effort to “force” the profiles into an assemblable position, introduces a variable error across profile sizes that can not be easily accounted for.

Design Improvement

Improvements to the design of the test assembly should be focused in two areas:

1. Reducing eccentricity

This might be pursued with the current assembly by manufacturing extra spacers to maintain the cylindricality of the assembly at the $\frac{1}{4}$ and $\frac{3}{4}$ locations along the shaft. These might be permanently installed to each outer PVC profile, allowing the same installation procedures, but helping maintain shape rather than allowing the profiles to spring in.

2. Increasing ease of assembly

This might be pursued with the current assembly by permanently fastening the spacers to the interior of each profile. This could be done with flush screws from outside of the profiles, into the spacers. Installation would then require several fasteners mating each exterior profile+spacer subassembly to the next subassembly in. This would significantly reduce the number of fasteners involved with assembly/disassembly, as well as eliminating many separate alignment operations. Significant time savings would allow for more reconfigurations and more testing per day on the water.

Appendix B: Manufacturing

Manufacturing the test assembly was a straightforward process. The chronological order of manufacturing processes was determined by the state of design completion and the arrival of materials. Arrival of materials was influenced by a snow storm which persisted in Seattle in the early weeks of February, delaying some materials.

Processes

1. Spacers
 - a. Waterjet spacer profiles from .75" delrin sheet
 - b. Sand rough edges
 - c. Drill spacer holes on mill
 - d. Tap by hand
2. PVC
 - a. Cut PVC to length with dropsaw
 - b. Scribe lengthwise halving lines with jig
 - c. Cut PVC in half with jigsaw
3. Radial Holes
 - a. Sand spacers to fit in PVC
 - b. Assemble one half at a time using plywood alignment jig
 - c. Use straps to hold profiles and spacers tightly together
 - d. Drill and countersink radial holes with hand drill and v-block
 - e. Tap by hand
4. Assembly
 - a. Test-assemble on R/V Light turbine
 - b. File/sand excess material to achieve fit

A Flow waterjet was used to cut the spacers from a sheet of 24"x36"x1/4" delrin. Unbeknownst to the machinist, the abrasive supply to the waterjet was clogged during this process. The cut was run at 20% speed to achieve separation. A poor surface finish resulted, but the spacers were recoverable with some sanding.

A two axis mill was used for non-radial drilling operations. Chuck clearance on larger spacers was maintained by using extra long bits.

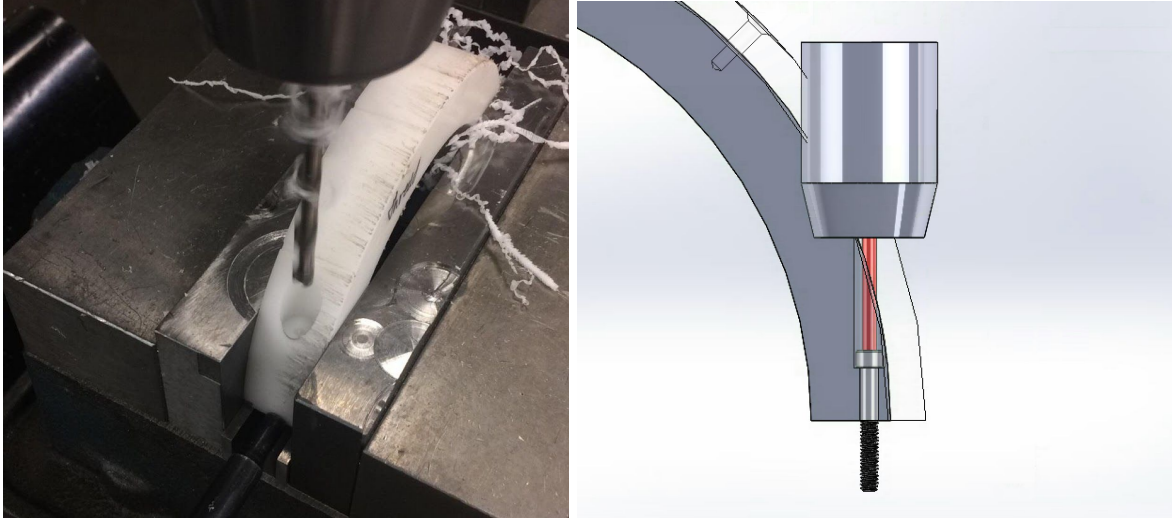


Figure A.9. Drilling spacers and interference estimate for the drill chuck clearance

A laser cutter was used to cut plywood for jigs for scribing profiles and constructing a radially drillable assembly. The first series of jigs positioned a straightedge along each PVC pipe for scribing, allowing for an accurate lengthwise parting cut. The second jig provided markings and holes in appropriate places such that one half of the assembly could be built at a time and held in place for drilling.

This jig was used to compose spacers and profiles in the proper places for the drilling of radial holes. Holes were drilled with a V block through layers of PVC into the baffle beneath, ensuring alignment. Countersinking was also performed by drill, tapping by hand. Further unexpected difficulties cropped up during this section of manufacturing. Residual stress in each PVC pipe caused the edges to curl in when cut in half. This introduced a certain variability to the assembly. Once assembled, strapped together, and drilled, the assembly was found to only be assemblable by mimicking the arbitrary forces and slight variations in part locations that were present during manufacturing.

Several other complications increased the difficulty of manufacturing. The size of the PVC itself proved to be a significant challenge. 12 and 16 inch PVC is too large to be cut on most shop tools, requiring improvisation and the use of hand tools. An additional difficulty came from the team's short manufacturing schedule. Researchers had 3 weeks from the design finalization until testing during which to manufacture the entire assembly. Some materials took a week or more to ship, which pinched manufacturing time. Finally, the 2019 winter has been one of the snowiest that the UW has seen in recent years, causing five days of campus closures. This limited access to tools and resources in the machine shop.

Despite these challenges, shopmasters Reggie Rocamora and Eamon McQuaide at the UW ME Machine Shop supplied incalculable aid during manufacturing, offering design ideas, manufacturing tips, and a magical space in which everything needed could be found.

Appendix C: Original Test Hierarchy

Experiment Name	Goal	Turbine Parameters	Method	Relative Priority
Data Acquisition Test	Make sure that all systems are go, that code works, and that there aren't any obvious hiccups	Standard shaft, 1 or 2 blades, 6° preset pitch, 10 cm chord, 1, 2, 3 TSR	U = 2 m/s TSR from 0 to 5 Increment by 0.5	Very High
1 bladed test, coarse	Study the effect of driveshaft geometry on a single blade throughout its cycle. Use coarse TSR range to determine range to investigate more finely. Serve as test run of clamshell geometry design.	All geometries, 1 blade, 6° pitch, 10 cm chord, 0 - 5 TSR, increment by 0.5	U = 1.5, 2, 2.5 m/s TSR from 0 to 5 Increment by 0.5	High
1 bladed test, fine	Study the effect of driveshaft geometry on a single blade throughout its cycle. Investigate a smaller TSR range with finer increments.	All geometries, 1 blade, 6° pitch, 10 cm chord	U = 1.5, 2, 2.5 m/s TSR TBD Increment by 0.1	High
0 bladed test	Study loads on driveshaft geometry without contributions from the blades, and gain insight into potential losses that may be occurring due to the geometry alone.	All geometries, 0 blades	U = 1.5, 2, 2.5 m/s TSR TBD Increment by 0.1	High
2 bladed test	Gain further understanding of relationship between blade count, driveshaft geometry, and structural loads	All geometries, 2 blades, 6° pitch, 10 cm chord	U = 1.5, 2, 2.5 m/s TSR TBD Increment by 0.1	Medium
Chord length test	Examine the impact of blade chord length on turbine performance and interactions between blades and wake	All geometries, 1 blade, 6° pitch, 10-15-20 cm chord	U = 1.5, 2, 2.5 m/s TSR TBD Increment by 0.1	Low
4 bladed test	Confirm our understanding of blade count, driveshaft geometry, and loads relationship	All geometries, 4 blades, 6° pitch, 10 cm chord	U = 1.5, 2, 2.5 m/s TSR TBD Increment by 0.1	Very Low
3 bladed test	Investigate "best of both worlds" blade count and performance in a field scale turbine	All geometries, 3 blades, 6° pitch, 10 cm chord	U = 1.5, 2, 2.5 m/s TSR TBD Increment by 0.1	Very low, requires machining new plates

Appendix D: Description of Data Analysis Methods

The data analysis performed for this experiment consisted of three main phases:

- Separation of the data into chunks based on TSR being tested
- Separation of TSR chunks into individual cycles
- Calculation of C_p values

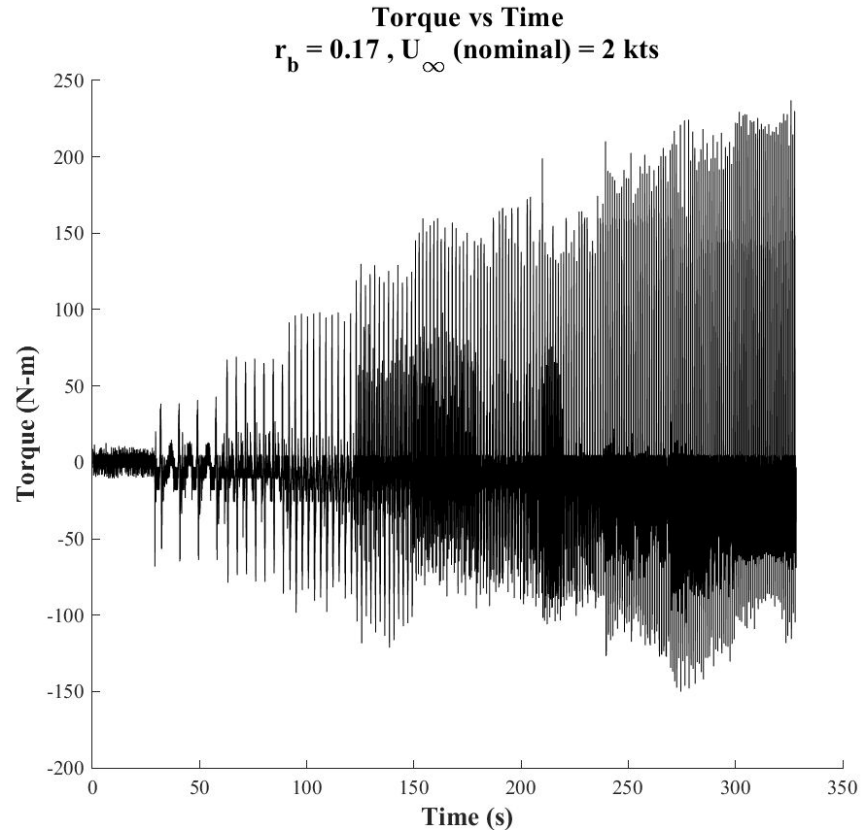


Figure A.10. Raw torque vs time data obtained from the data acquisition system.

Torque, latitude, longitude, and time data for an entire test (a single shaft size at a single vessel speed, tested across all TSRs) were obtained from the data acquisition system. An example of raw torque data is given in Figure A.10. As no information was available regarding the actual speed of the turbine during the experiment, the rate of rotation is assumed to be the nominal value specified at the input. Additionally, since the exact time at which the TSR was altered after each 30 second interval was not reported by the data acquisition system, these time splits were recorded manually in order to make sorting of the data easier during post processing.

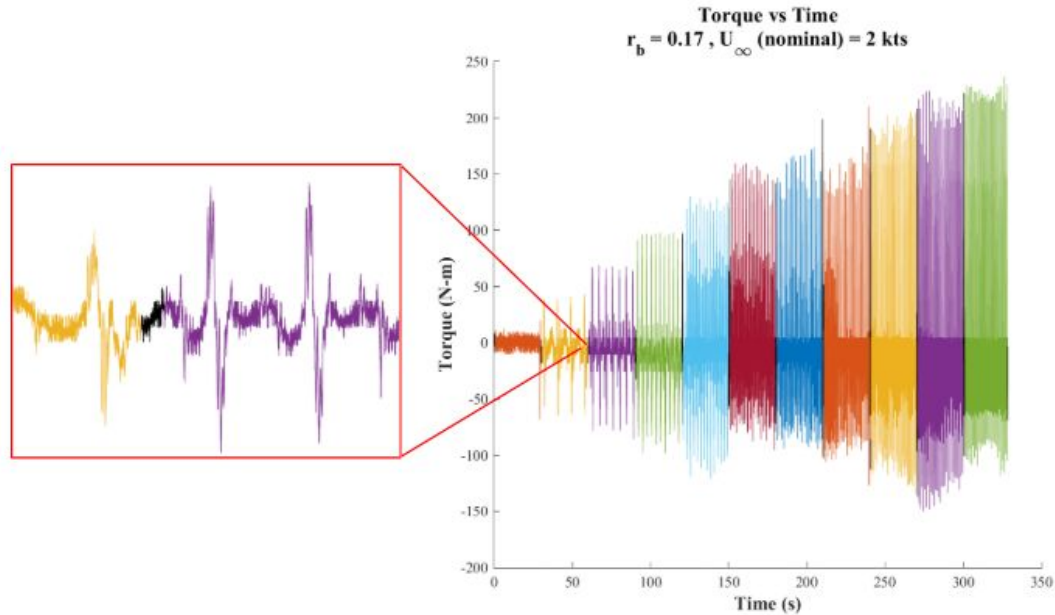


Figure A.11. The previous torque data sorted according to the TSR being tested in each 30 second interval. The black portion of the curve in the magnified view represents data during a TSR transition that was trimmed away.

To separate the raw data for a single test by TSR, torque and time data were indexed according to the previously recorded time splits. In order to account for TSR transition periods where the angular velocity of the turbine might not be constant, a half second of data before and after each time split was removed. The resulting torque data sorted by TSR is shown in Figure A.11.

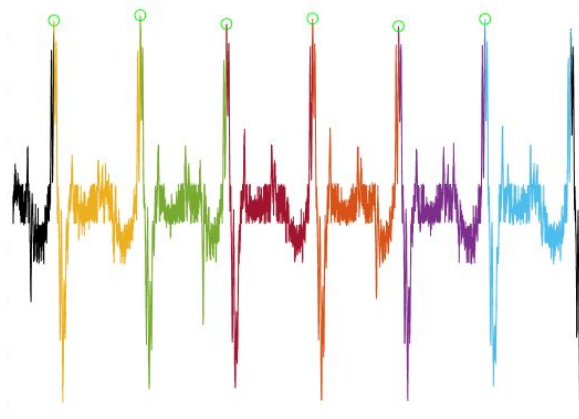


Figure A.12. An example of torque data for a TSR interval split into its component cycles. Peak torques that were identified as the beginning of each cycle are circled. Portions of the data that do not correspond to an integer rotation were trimmed away and are colored black.

For each TSR interval, the corresponding torque data were further split into individual cycles. As blade azimuthal position was not known, cycles were identified through repeatable patterns in the torque data. The first peak torque in the TSR interval was identified and set as the beginning of the first cycle for that interval. Using the known nominal rotation rate of the turbine for that TSR, the time per rotation was calculated. Using this time per cycle, the data were trimmed to be an integer number of turbine rotations so as to avoid biasing the results by including incomplete rotations. Finally, using the time per rotation (and allowing for small variations from nominal cycle time), the beginning of each subsequent cycle was found by identifying the next peak torque within the expected time window. This process is depicted in Figure A.12.

With the data fully sorted, cycle metrics can now be calculated. The average free stream velocity is obtained from the GPS data for the vessel for the entire test. The details of this process, as well as a discussion of its limitations, can be found in Appendix E. The resulting free stream velocity is assumed to be constant over the entire test. The instantaneous coefficient of performance, C_p , is calculated at every data point. Cycle average performance is calculated by averaging the obtained C_p values for each cycle.

As mentioned in the results section of this report, true phase average results cannot be obtained since the azimuthal position of the blade is not known. However, “pseudo-phase average” results can be calculated by assigning a phase of 0° to the peak torque that was used to identify the beginning of each cycle (see Figure A.12). Since actual cycle length varies slightly, phase average performance is obtained by interpolating the performance data for each cycle onto a common phase vector, and averaging those interpolations.

Appendix E: Methods for Determining Vessel Velocity

Many methods were used to attempt to estimate the vessel’s actual speed during the experiment. While nominal vessel speeds of 2 kts and 4 kts were maintained by the vessel captains, small variability in vessel speed could significantly impact C_p values obtained. In the absence of an acoustic Doppler velocimeter (ADV), latitude and longitude data obtained via GPS during the test were used to estimate the vessel velocity. Change in latitude and longitude were converted to meters travelled, and from this the time data were used to estimate the vessel velocity.

Difficulties were encountered when attempting to estimate an average velocity from the GPS data. Initial methods sought to fit a line or polynomial to position data for each TSR interval during a test (i.e. all data collected at a given vessel speed, shaft size, and TSR), and differentiate this polynomial to analytically obtain the vessel velocity during each TSR in that test. However,

use of this method resulted in large variations in average vessel speed of up to 0.5 kts across tests. This seemed suspect, as the vessel captains were confident that variations in velocity were only +/- 0.1 kts from the nominal value. Another method involved splitting the position data for the entire TSR interval into smaller segments, fitting a line to each segment, and averaging the slopes of those lines to find the average velocity. This method was found to be extremely sensitive to the size of the line segments used, making it difficult to know what the whether the result obtained was the “true” average velocity. These challenges persisted when these methods were applied to the entire test (i.e., all data collected at a given shaft size and vessel speed, across the entire TSR range). Ultimately, both of these methods for estimating an actual vessel speed were deemed to be no more accurate than simply assuming a nominal vessel speed.

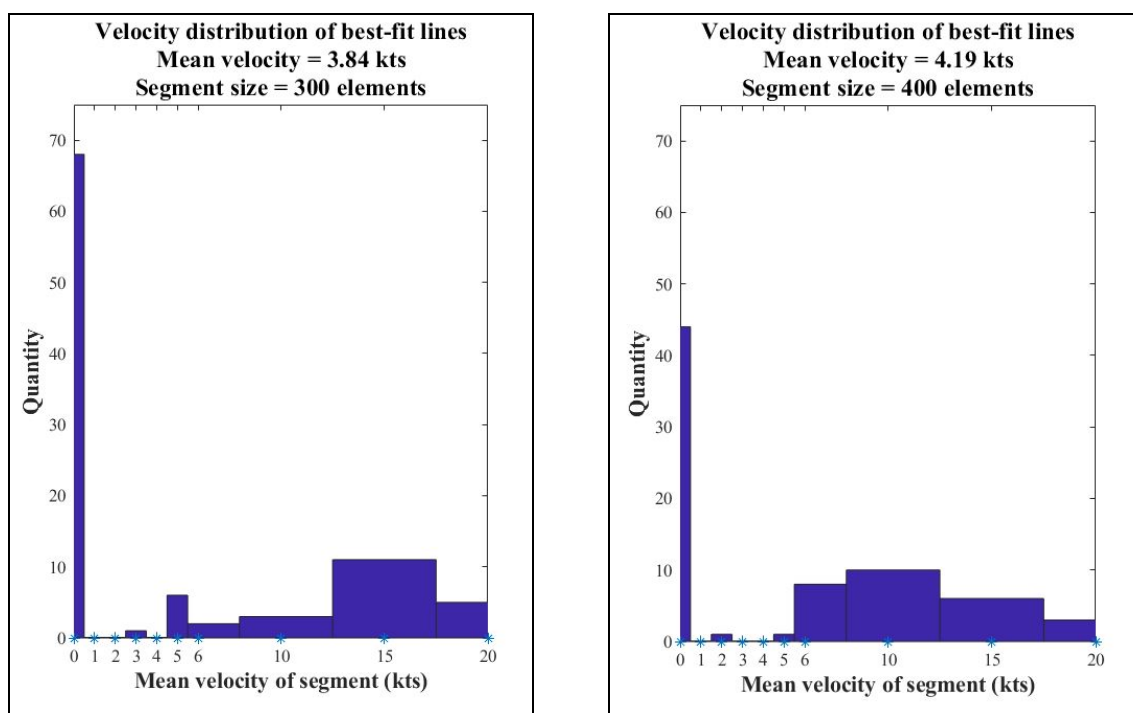


Figure A.13. Two histograms of line segment velocity of a TSR interval, each using a different line segment size.

The main problem with the methods previously described lies in the sampling rate of the GPS onboard the vessel. Unlike the other sensors, the GPS does not log the vessel’s position at 1000 Hz. Instead, the vessel’s latitude and longitude are updated roughly every half second. At all instances between updates, the GPS reports the previous position. This complicates line fitting, as segments of the position data as received from the GPS report the vessel either moving very quickly or not moving at all. The histograms in Figure A.13 illustrate this unrealistic distribution, as well as its dependence on the size of the line segments used for fitting.

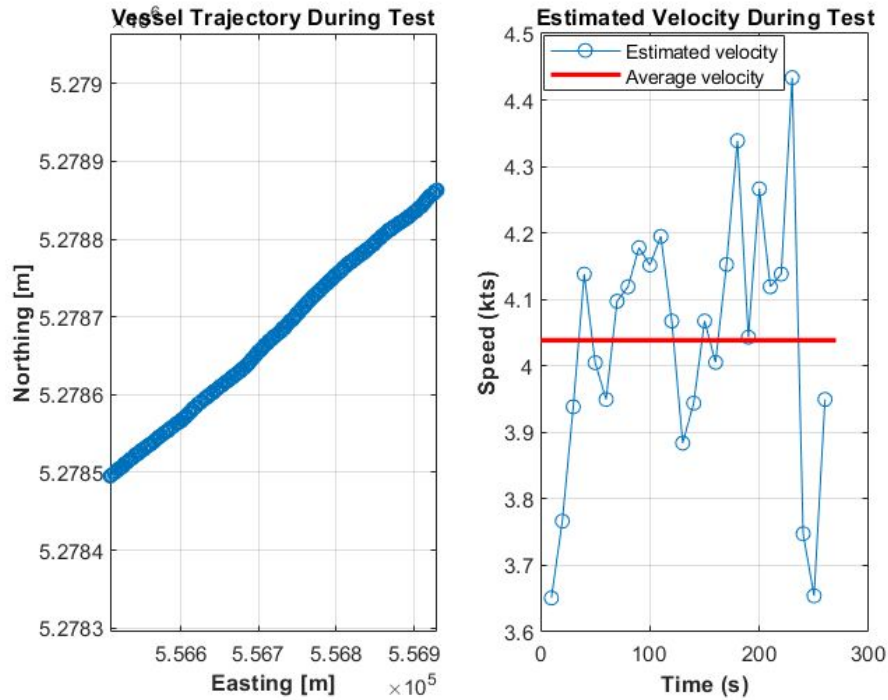


Figure A.14. Vessel trajectory and corresponding velocity approximation using a coarse time vector.

The final method used to estimate vessel speed interpolated the position data from the GPS for the entire test onto a coarse time vector of 10 second increments. This method is visualized in Figure A.14. The resulting smoothed position data were numerically differentiated to obtain the velocity over each 10 second interval, and the average velocity obtained. Use of a coarse time vector helped to smooth the low update rate of the position data, and the resulting variations in calculated average velocity were in most cases within the bounds described by the vessel captains. However, the coarse time vector imposed other restrictions on accuracy, as only the average vessel speed over the entire TSR range tested (rather than the average speed for each 30 second TSR increment) could be reliably estimated. Use of a time vector with 10 second increments did not provide a high enough resolution to reliably estimate the average velocity of each 30 second TSR interval, and time vectors of smaller increments proved to introduce more variability. As such, the average velocity for each test was used in to calculate C_p and TSR values.